PAPER • OPEN ACCESS

Trends in runaway electron plateau partial recombination by massive H_2 or D_2 injection in DIII-D and JET and first extrapolations to ITER and SPARC

To cite this article: E.M. Hollmann *et al* 2023 *Nucl. Fusion* **63** 036011

OPEN ACCESS
IOP Publishing | International Atomic Energy Agency
Nuclear Fusion
Nucl. Fusion **63** (2023) 036011 (13pp)
https://doi.org/10.1088/1741-4326/acb4aa

Trends in runaway electron plateau partial recombination by massive H_2 or D_2 injection in DIII-D and JET and first extrapolations to ITER and SPARC

E.M. Hollmann[1,*], L. Baylor[2], A. Boboc[3], P. Carvalho[3], N.W. Eidietis[4], J.L. Herfindal[2], S. Jachmich[5], A. Lvovskiy[4], C. Paz-Soldan[6], C. Reux[7], D. Shiraki[2], R. Sweeney[8] and JET Contributors[a]

[1] University of California—San Diego, 9500 Gilman Drive, La Jolla, CA 92093-0417, United States of America
[2] Oak Ridge National Laboratory, PO Box 2008, Oak Ridge, TN 37831, United States of America
[3] CCFE, UKAEA, Culham Science Centre, Abingdon OX14 3DB, United Kingdom of Great Britain and Northern Ireland
[4] General Atomics, PO Box 85608, San Diego, CA 92186-5608, United States of America
[5] ITER Organization, Route de Vinon sur Verdon, 13115 St-Paul Lez Durance, France
[6] Department of Applied Physics, Columbia University, New York, NY 10027, United States of America
[7] CEA, IRFM F-13108 St-Paul Lez Durance, France
[8] Massachusetts Institute of Technology, 77 Massachusetts Ave, Cambridge, MA 02139, United States of America

E-mail: hollmann@fusion.gat.com

Received 29 August 2022, revised 16 December 2022
Accepted for publication 19 January 2023
Published 2 February 2023

Abstract

Experimental trends in thermal plasma partial recombination resulting from massive D_2 injection into high-Z (Ar) containing runaway electron (RE) plateaus in DIII-D and JET are studied for the purpose of achieving sufficiently low electron density ($n_e \approx 10^{18} m^{-3}$) to increase RE final loss MHD levels. In both DIII-D and JET, thermal electron density n_e is found to drop by $\sim 100\times$ when the thermal plasma partially recombines, with a minimum at a vacuum vessel-averaged D_2 density in the range 10^{20}–$10^{21} m^{-3}$. RE effective resistivity also drops after partial recombination, indicating expulsion of the Ar content. The n_e level after partial recombination is found to increase as RE current is increased. The amount of initial Ar in the RE plateau is not observed to have a strong effect on partial recombination. Partial recombination timescales of order 5 ms in DIII-D and 15 ms in JET are observed. These basic trends and timescales are matched with a 1D diffusion model, which is then used to extrapolate to ITER and SPARC tokamaks. Within the approximations of this model, it is predicted that ITER will be able to achieve sufficiently low n_e values on time scales faster than expected RE plateau vertical drift timescales (of order 100 ms), provided sufficient D_2 or H_2 is injected. In

[a] See Mailloux *et al* 2022 (https://doi.org/10.1088/1741-4326/ac47b4) for the JET Contributors.
[*] Author to whom any correspondence should be addressed.

SPARC, it is predicted that achieving significant n_e recombination will be challenging, due to the very high RE current density. In both ITER and SPARC, it is predicted that achieving low n_e will be easier with Ar as a background impurity (rather than Ne).

Keywords: tokamak, runaway electrons, ITER

(Some figures may appear in colour only in the online journal)

1. Introduction

In future large current tokamaks like ITER there is the possibility of severe localized wall damage due to post-disruption runaway electron (RE) wall strikes [1–3]. Present research is investigating the possibility of reducing RE wall damage by massive impurity injection into the RE beam (or 'plateau') in the form of a gas jet or shattered cryogenic pellets [4–6]. Massive impurity injection into the RE plateau is typically referred to as 'second injection' to distinguish from 'first' injection for thermal quench (TQ) heat load mitigation and/or current quench (CQ) force and heat load mitigation. Typically, neon (Ne) or argon (Ar) are used as the main radiating impurity in first injection, to increase radiation rates and help reduce conducted heat loads (additional H_2 or D_2 gas can be added at this time also). Ar (or Ne) can also be used for second injection, and has been observed to cause rapid added dissipation of RE kinetic and magnetic energy in DIII-D [4]. However, the potential effectiveness of Ar injection for mitigating RE damage effectively in future devices is uncertain, due to relatively poor (often $< 10\%$) impurity assimilation of Ar [4, 7, 8] into the RE plateau, increased vertical instability growth rate of the RE current channel [9, 10], and very slow mixing timescale of Ar ions into the RE plateau [11].

A related approach being investigated to reduce RE wall damage is massive second injection of low-Z species, such as deuterium (D_2) or hydrogen (H_2). RE wall damage depends on RE beam current, final wall strike wetted area, and time scale of the final loss [12]. RE beam current dissipation is reduced by low-Z species injection, (which is undesirable); however, vertical instability growth rate is reduced (which is desirable), as is magnetic-to-kinetic energy conversion (which is also desirable) [13]. Also, low-Z second injection appears to cause reduced final loss time scale (which is undesirable) and increased wall strike wetted area (which is desirable) [14–16]. The source of these differences in final loss time scale and wetted area appear to stem dominantly from a much larger final loss MHD amplitude δB following low-Z injection [14]. The origin of the larger final loss MHD amplitude in the low-Z case is not fully understood at present. It is possible that the removal of high-Z impurities from the RE beam can contribute to the larger MHD amplitude by lower RE resistivity. However, helium second injection, which removes high-Z impurities from the RE beam, but does not cause partial volume recombination (as D_2 and H_2 injection tend to), and does not seem to access large δB, seems to contradict this hypothesis [16]. Alternately, it is hypothesized that plasma partial recombination, which results in a very large Alfven velocity and very small Alfven timescale, could be responsible for the large observed δB. Although not confirmed, this hypothesis motivates the study of whether or not it will be possible to sufficiently recombine RE plateau background plasmas in future large tokamaks using massive D_2 or H_2 injection.

In the present work, experimental trends are studied, looking at experiments on low-Z (D_2) injection into RE plateaus in DIII-D [16] and JET [17] tokamaks. To predict expected trends in ITER [2] and SPARC [18], a 1D diffusion model is used [10, 19]. The main result of the study is that sufficient RE plateau recombination is expected to be possible in ITER but challenging in SPARC, when using realistic injection parameters. The ITER recombination timescales following massive H_2 or D_2 injection are predicted (within the approximations of this model) to be sufficiently fast for use in ITER, providing sufficiently large quantities of H_2 or D_2 are injected. Achieving sufficient RE plateau recombination is predicted to be more difficult at higher plasma current and may be challenging to achieve in the worst-case scenario of a 10 MA RE plateau in ITER. In both ITER and SPARC, achieving sufficient recombination is predicted to be more difficult if using Ne first injection (rather than Ar first injection, as is often used in present devices), dominantly due to slower Ne molecular recombination rates. Increasing either the Ne or Ar first injection quantity is predicted to slowly make partial recombination more challenging.

This paper is organized as follows: section 2 gives an overview of experimental data used from DIII-D and JET. Section 3 describes the 1D diffusion model used to interpret the experimental data and extrapolate to ITER and SPARC. Section 4 discusses the time scale of electron density drop and how this is used to constrain the model neutral diffusion coefficients. Section 5 compares data and modeling on the equilibrium electron density achieved after partial recombination. Section 6 discusses the effect of RE plateau current on partial recombination, while section 7 deals with the effect of initial Ar (or Ne) number. Section 8 discusses future work, and section 8 gives a brief conclusion. appendix describes the changes made to the 1D diffusion model for this work.

2. Experimental background

Time traces from a typical DIII-D experiment are shown in figure 1. The thermal plasma current is ramped up to 1.2 MA, figure 1(*a*), and the thermal plasma is then disrupted by rapid injection of Ar first injection at time 1200 ms in figure 1(*a*). Rapid second injection of D_2 then occurs at time 1450 ms. Finally, around time 1800 ms, the RE plateau drifts vertically into the wall and is lost in a final loss magneto-hydrodynamic

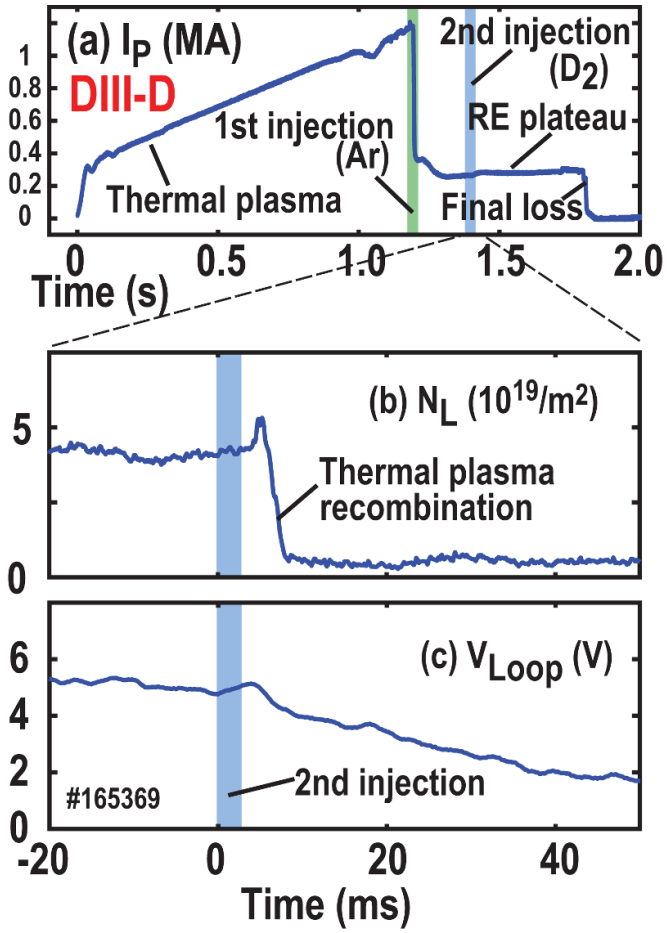

Figure 1. Sample time traces showing recombination of RE plateau following massive D_2 gas second injection in DIII-D showing: (*a*) plasma current (whole shot), (*b*) electron line density (zoomed in time), and (*c*) loop voltage (zoomed in time) as a function of time for DIII-D shot #165369. Time in (*b*) and (*c*) is shown relative to second injection impact time $t = 1405$ ms.

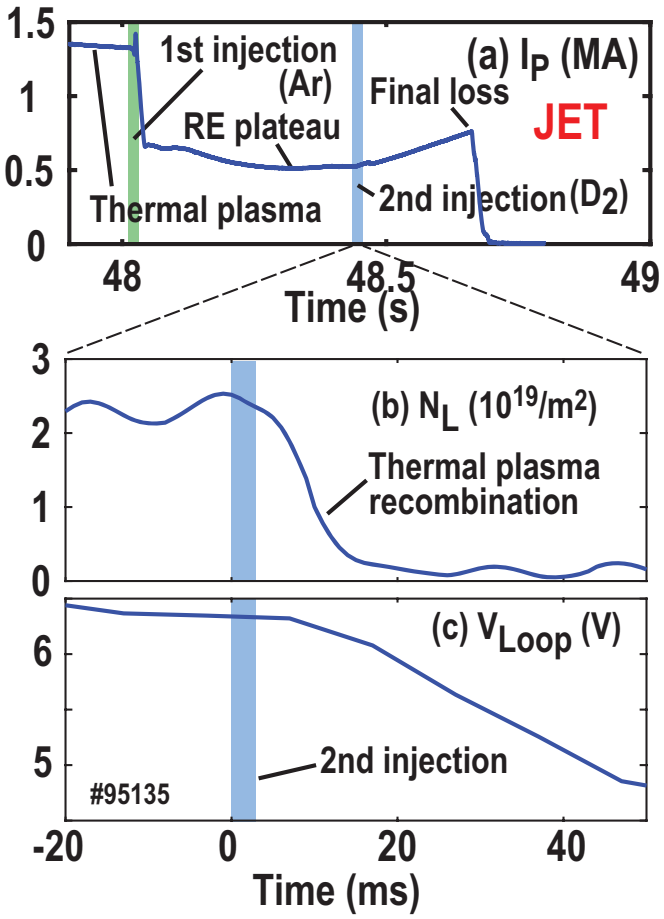

Figure 2. Sample time traces showing recombination of RE plateau following massive D_2 gas second injection in JET showing: (*a*) plasma current, (*b*) electron line density (zoomed in time), and (*c*) loop voltage (zoomed in time) as a function of time for JET shot #95135. Time in (*b*) and (*c*) is shown relative to second injection impact time $t = 48.435$ s.

(MHD) event (this vertical instability is programmed here into the control system to simulate the uncontrolled vertical loss expected in ITER). Rapid (<10 ms) partial recombination of the background thermal plasma following the second injection can be seen in the line-integrated electron density measured with a midplane interferometer chord, figure 1(*b*). The partial recombination results in a purge of background Ar out of the plasma, resulting in a lower RE resistivity and a drop in the plasma loop voltage, figure 1(*c*).

Time traces from a typical JET experiment are shown in figure 2. The subfigures (*a*)–(*c*) show the same variables as in figure 1 and exhibit qualitatively similar behavior, although with longer time scales. In DIII-D, first injection of 14 Torr-L of Ar is delivered via a solid cryogenic pellet; in JET, 23–323 Torr-L of Ar is injected with massive gas injection (MGI). In the shots studied here, massive second injection of D_2 is done by MGI in DIII-D and by shattered pellet injection (SPI) in JET.

The main diagnostic used for experimental data shown in this work to diagnose RE plateau background plasma recombination is the line-integrated midplane electron density from a horizontal midplane IR interferometer in DIII-D [20], and from a vertical far infra-red (FIR) polarimeter (using the Cotton–Mouton effect) in JET [21]. In the case of the JET data, the polarimeter data is time shifted to account for a slight delay and is also amplitude scaled to match fast interferometer data pre-disruption; this technique is used to obtain the most accurate possible line-integrated electron density without fringe skips [21]. For both DIII-D and JET, line-integrated density measurements have noise floors in the vicinity of 10^{18}m^{-2}.

Some radiated power data is also shown, in figures 5(*d*) and 6(*d*). For DIII-D, inverted bolometer array data is used initially (for times prior to D_2 injection). For times after D_2 injection in DIII-D, it is simply assumed that radiated power is proportional to line-integrated central Ar-II line brightness, since the radiated power evolution in the DIII-D experiments occurs too quickly to track with the slow foil bolometers. In JET, bolometer array data is used exclusively and is sufficiently fast to track the recombination process. Inversions for JET use a simple weighted average over different chords, while in DIII-D a smoothed inversion forcing poloidal and toroidal symmetry about the RE beam magnetic axis is used.

3. Diffusion model

Interpretive modeling of experimental results and extrapolation to ITER and SPARC are done here with a 1D diffusion model [10, 19]. This model approximates the actual 3D toroidal geometry with a 1D cylindrical (radial) diffusion solver. Second injection of either MGI or SPI is approximated as an edge ($\rho = 1$) deposition of impurities; this is experimentally supported, as no clear sign of direct radial penetration of either MGI or SPI injected impurities is observed experimentally [6]. The neutral deposition is taken to be Gaussian in time with a narrow 1 ms full width at half maximum; since this deposition time is short compared with diffusion time scales, the exact width is not found to be important. The ion radial diffusion coefficient is approximated as $D_i = 2$ m^2 s^{-1}, based on experimental measurements [11], and is assumed to be independent of plasma parameters and constant in space and time. Neutral radial diffusion coefficients are calculated from first principles, with an empirical enhancement factor due to convective cells, as discussed below. Charge states up to 4+ are included for the high Z species (Ar or Ne), as are the hydrogenic molecular ions D_2^+, D_3^+, and ArD^+ (or NeD^+). A single thermal temperature profile is assumed as a function of radius for all non-RE species (thermal electrons, neutrals, and ions). An earlier version of the 1D diffusion model used separate temperature profiles for each species, but this was found to considerably add to computational overhead, with little effect on the simulation results: due to the very low thermal plasma temperatures, equilibration times between different species are extremely short, so simulated temperatures of thermal electrons, ions, and neutrals were typically found to be within 20% of each other [10]. REs are modeled with a kinetic test particle model using a mono-energy/mono-pitch approximation [10, 22]. The value of the toroidal electric field is central to this model, as the electric field accelerates electrons in the toroidal direction, reducing pitch angle, increasing energy, and increasing current density. The model does not contain an Ampere–Faraday solver to model the radial profile of toroidal electric field self-consistently; instead, toroidal electric field is just assumed to be constant as a function of radius and is scanned up or down in the RE solver to try to maintain the chosen total toroidal plasma current. A max slew rate of 0.4 V ms^{-1} in loop voltage is used in the solver when scanning the toroidal electric field.

The modifications done to this model for the present work are: (a) adding the D^- ion (to improve accuracy of molecular recombination rate), (b) adding the capability to simulate H_2 injection (instead of D_2), and (c) adding the capability to use Ne (instead of Ar) as the initial high Z ion. These changes are described in appendix. Ne, when compared with Ar, has faster diffusion, lower RE stopping power, lower radiation rates (for low temperature plasma), and slower molecular recombination. H, when compared with D, has similar reaction cross sections, but faster radial diffusion.

For DIII-D and JET simulations, experimental injected particle quantities are used. For ITER and SPARC, rough guesses for atom numbers present in the RE plateau are used, based on expected initial discharge parameters and first injection quantities. Particles released or absorbed from the walls during the TQ are ignored in all cases. Presently, ITER is intending to use H_2 injected into a Ne-containing RE plateau, while SPARC is likely to use D_2 injected into a Ne-containing RE plateau. The ITER plan to use H_2 is motivated by its faster mixing time and expected better disruption mitigation effectiveness, while the SPARC plan to use D_2 is motivated by hydrogen isotope control in the discharges that follow. To illustrate trends from different species, the simulations shown in this paper are not restricted to presently planned future species combinations, i.e. both H_2 and D_2 second injection, and both Ar and Ne first injection are simulated for ITER and SPARC. The initial pre-disruption plasma in ITER is assumed to have a typical D content of 6×10^{22} D atoms ($=2 \times 10^3$ Torr-L D), which carries over into the RE plateau. The typical initial Ar (or Ne) content of the ITER RE plateau (left over from first injection) is assumed to be 8×10^{21} atoms ($=270$ Torr-L). In SPARC, the initial D content is assumed to be 660 Torr-L D, while the initial Ar (or Ne) content left over from first injection is assumed to be 33 Torr-L.

The 1D diffusion model indicates that the observed RE plateau recombination level (equilibrium cold electron density) is dominantly set by a balance between RE impact ionization and volume recombination of molecular ions. This is illustrated in figure 3 which shows simulated (*a*) free electron density, (*b*) thermal plasma power balance, and (*c*) thermal plasma electron balance vs time (with time $t = 0$ corresponding to the second injection time). D_2 injection into Ar in ITER is shown; the dominant processes are predicted to be similar in JET, DIII-D, and SPARC. Power enters the cold plasma from RE collisions on free and bound electrons, red curve in figure 3(*b*). The RE stopping power drops in time due to the loss of Ar out of the plasma volume. Initially, the RE stopping power is dominantly balanced by thermal radiation (line radiation due to thermal electron impact on Ar ions). Other dominant power loss terms are RE radiation and neutral cooling. As the plasma cools, neutral cooling rises and becomes the dominant heat loss mechanism, shown by the blue curve in figure 3(*b*). Here, 'neutral cooling' refers to heat carried to the vessel wall by D atoms and D_2 molecules as kinetic and internal (ro-vibrational) energy. 'RE radiation' refers to line radiation resulting from direct RE impact excitation of atoms and ions (bremsstrahlung is much smaller and can be neglected here).

In terms of cold plasma particle (electron) balance: as shown in figure 3(*c*), ionization of cold plasma is dominated by RE impact, which is balanced by a mixture of radial plasma transport to the wall and atomic recombination initially. Atomic recombination refers to all volume recombination channels of atomic ions (radiative, three-body, and dielectronic). As the plasma composition evolves, however, molecular recombination becomes dominant, shown by the blue curve in figure 3(*c*). Molecular recombination refers to all volume recombination channels involving the modeled molecular ions (D_2^+, D_3^+, D^-, and ArD^+). Charge-exchange

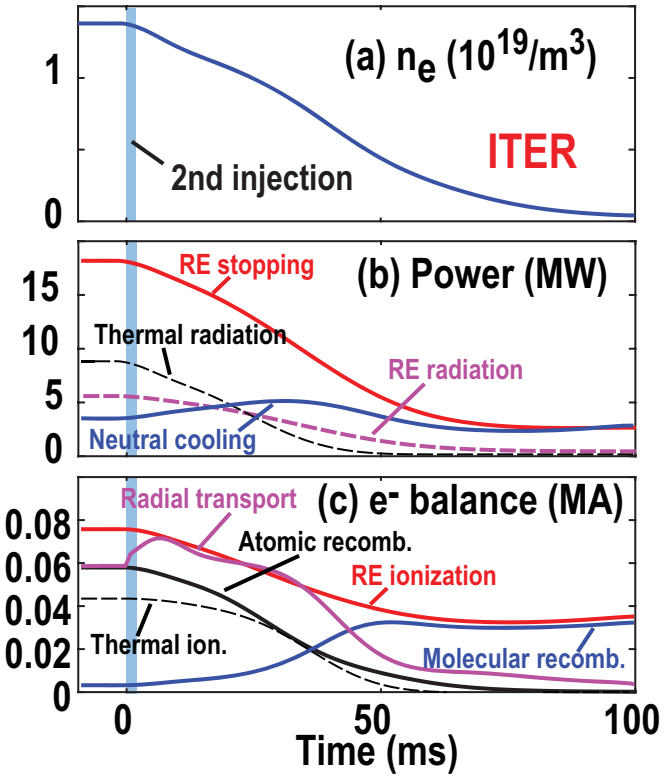

Figure 3. Simulated RE plateau thermal plasma recombination in ITER showing (*a*) profile-average electron density, (*b*) thermal plasma power balance, and (*c*) thermal plasma free electron balance as a function of time. Simulation is done for ITER $I_P = 5$ MA target, 5×10^3 Torr-L D_2 into 270 Torr-L background Ar, with neutral diffusion coefficients scaled by $D_0 = 5$. Time is plotted relative to second injection time.

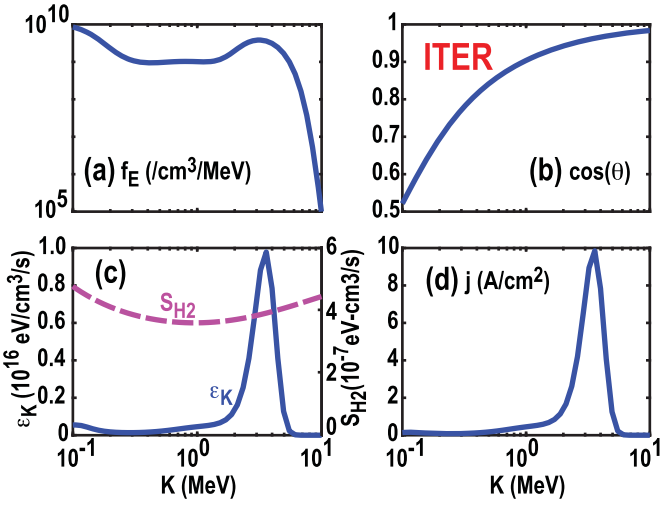

Figure 4. Distribution function simulated for ITER prior to second injection showing (*a*) energy distribution function, (*b*) pitch angle, (*c*) RE power deposition density ε_K and (RE on H_2) stopping power S_{H_2}, and (*d*) current density j as a function of energy. Simulation has number of Ar atoms = 270 Torr-L, and $I_P = 5$ MA. Neutral diffusion scaling is $D_0 = 5$. Results are shown at minor radius $\rho = 0.8$.

recombination between different ions and neutrals is included in the model, but does not cause any net change in cold electron density, so does not appear in figure 3(*c*).

Since the dominant power balance dynamic in the recombining plasma is RE impact heating balanced by neutral cooling, it follows that the RE heating term and neutral transport rate are two crucial elements for modeling the recombination correctly. Uncertainties in the neutral transport will be discussed in section 4.

RE heating is set by the RE energy distribution function, which is partially constrained by the plasma current. A sample simulated energy distribution function for ITER is shown in figure 4(*a*), and corresponding pitch angle, stopping power, and current density as a function of RE kinetic energy are shown in figures 4(*b*)–(*d*). These simulations use the kinetic RE solver within the 1D diffusion model used here [10]. In figure 4(*c*) most of the energy deposition is predicted to come from REs in the 2–5 MeV kinetic energy range. The uncertainty resulting from different model RE energy distribution functions will be discussed in section 5. The pitch angle shown in figure 4(*b*) is relative to the toroidal direction; the kinetic model used here does not include the actual helical structure of the magnetic field.

4. Recombination time scale

Measured recombination time scales are valuable because they serve as a strong constraint on neutral diffusion time. In the 1D diffusion model used here, the radial neutral diffusion coefficients are calculated from first principles, from the first-order expansion of Chapman–Enskog theory [23], but an empirical correction factor (applied equally all neutral diffusion coefficients) is used to approximate the enhancement resulting from large-scale convective cells. Numerical simulations made for low pressure gas in inertial confinement fusion chambers suggest an enhancement factor $D_0 = 2.3$ [24]. However, better matching of observed DIII-D and JET recombination time scales is typically obtained here using slightly higher values $D_0 \approx 3 - 9$, so a higher value $D_0 = 5$ is used in this work for extrapolating to ITER and SPARC.

Figure 5 shows an example of recombination time scales observed in DIII-D showing time traces of (*a*) profile-averaged free electron density, (*b*) plasma current, (*c*) loop voltage at wall, and (*d*) radiated power. The solid blue and dashed blue curves show simulations with $D_0 = 1$ (unscaled neutral diffusion) with evolving REs (where the kinetic solver runs simultaneously with the diffusion solver) or 'frozen' REs, where the energy distribution function is locked at all radii to the initial ($t = 0$) values, to evaluate the effect of changes in the distribution function on the recombination time scale. Changes in f_E have only a small predicted effect on the recombination timescale. The simulated initial electron density in figure 5(*a*) does not match the measurement perfectly, as agreement between these two numbers is not required by the model; the model varies loop voltage to try to best match to experimental I_P, but

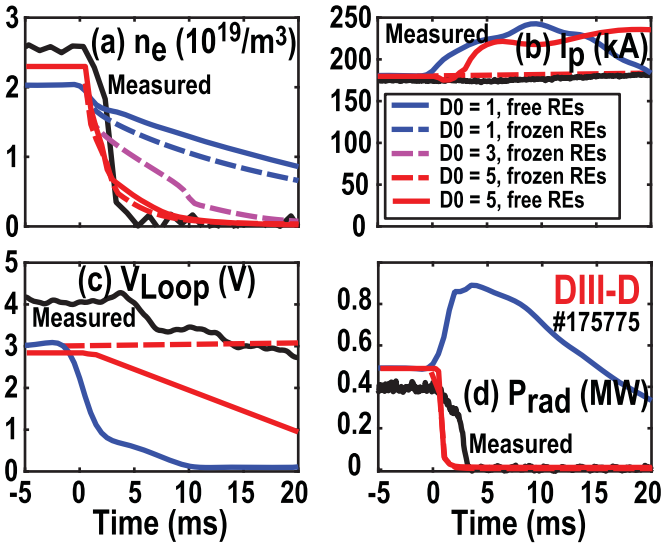

Figure 5. Time traces of RE plateau thermal plasma recombination in DIII-D showing (*a*) profile-average electron density, (*b*) plasma current, (*c*) loop voltage, and (*d*) radiated power as a function of time. Time is plotted relative to second injection time. Second injection is 500 Torr-L D_2 into plasma containing 15 Torr-L of Ar. The first four cases are all started at time $t = 0$ with the same equilibrium case ($D_0 = 1$, free REs), while the last case is started at $t = 0$ with a different equilibrium case ($D_0 = 5$, free REs).

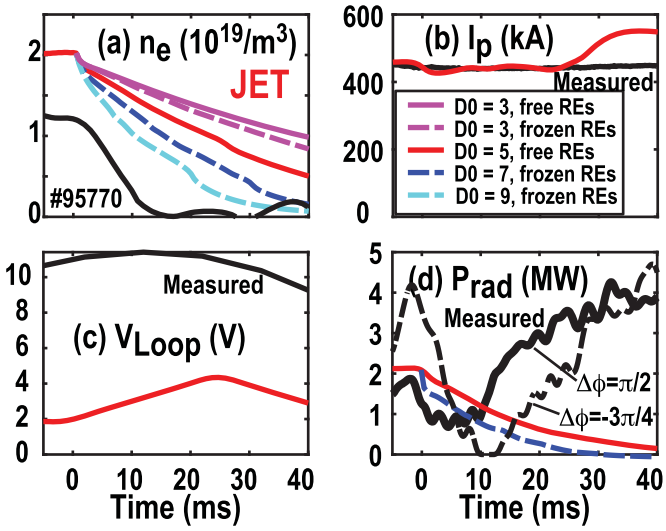

Figure 6. Time traces of RE plateau thermal plasma recombination in JET showing (*a*) profile-average electron density, (*b*) plasma current, (*c*) loop voltage, and (*d*) radiated power as a function of time. Time is plotted relative to second injection impact time $t = 48.238$ s. Second injection is 2400 Torr-L D_2 into plasma containing 63 Torr-L of Ar. Toroidal angles $\Delta\phi$ in (*d*) are relative to SPI injection location.

does not attempt to match initial n_e. Focusing on the timescale of the electron density drop, the measured electron density drop has a timescale (peak to $1/2$ max) of approximately 2.6 ms, while the simulation with $D_0 = 5$ gives 2.1 ms and the simulation with $D_0 = 3$ gives 4.8 ms. So the best fit D_0 is somewhere between 3 and 5 for this shot. In terms of plasma current and loop voltage evolution, freezing the REs (and current and loop voltage) actually matches the data better than allowing the current and loop voltage to evolve in the kinetic model for this shot. Radiated power, figure 5(*d*) is seen to drop quite rapidly (on similar timescales to the electron density drop), in better agreement with higher diffusion scaling $D_0 \sim 5$.

Figure 6 shows time traces of RE plateau thermal recombination in JET, with the same panels as in figure 5. In figure 6(*a*), the electron density recombination time scale (peak to $1/2$ max) is 8 ms, which is reasonably well-matched by $D_0 = 9$. As for DIII-D, changes in f_E are not predicted to strongly affect the electron density recombination rate, as can be seen from comparing dashed and solid magenta curves in figure 6(*a*). One difference from DIII-D is that the initial loop voltage is fairly well predicted in DIII-D, but poorly predicted in JET. This could be due to the more dynamic situation in JET, where the RE beam is not controlled vertically (as opposed to DIII-D, where vertical position control is maintained, even after second injection). Also, the radiated power is observed to rise in JET following D_2 second injection, while both the simulations and DIII-D data indicate a drop in radiated power. The cause of these discrepancies is not understood at present. Large rotating toroidal asymmetries have been observed in impurity density in RE plateaus in DIII-D [11], but these do not appear to be able to fully account for the JET radiated power discrepancy, as seen in the data from two toroidally spaced bolometer arrays in figure 6(*d*). The solid black curve corresponds to radiated power estimated from the vertical array in JET Octant 3 (at counter-clockwise toroidal separation $\Delta\phi = \pi/2$ from the SPI injector), while the dashed black curve corresponds to radiated power estimated from the horizontal array in JET Octant 6 (at toroidal sepration $\Delta\phi = -3\pi/2$ from the SPI injector). Although significant differences can be seen at early times after SPI injection ($t \sim 15$ ms), both indicate large radiated power at later times ($t \sim 40$ ms) when the injected D_2 gas can be expected to be more uniformly mixed toroidally.

Figure 7 shows time traces of predicted RE thermal plasma partial recombination in ITER, with same variables plotted as in figure 5. In figure 7(*a*) the red curve shows D_2 injection into an Ar-containing RE plateau, while the blue curve shows H_2 injection into a Ne-containing RE plateau.

The horizontal magenta band in figure 7(*a*) marks a rough threshold for sufficient 'recombination'. It is not known at present what the threshold is at which large-scale global MHD access will occur in ITER or SPARC during the RE plateau final loss instability. In present experiments, it appears that $n_e \approx 10^{18}\text{cm}^{-3}$ typically constitutes a sufficiently low electron density to allow the formation of very large, brief final loss events. Therefore, for the purposes of discussion in this paper, the rough guess of $n_e \approx 10^{18}\text{m}^{-3}$ is used as the upper bound for what is considered a sufficiently recombined RE plateau thermal plasma.

The vertical loss event (VDE) impact time (~100 ms) indicated in figure 7(*b*) for a low-Z ITER RE plateau is only a rough guess. For standard (high-Z) RE plateaus, it is expected to be of order 50–100 ms [25], so for low-Z plateaus, where the plasma resistivity is dropping as the gas enters the plasma, the VDE impact time can be expected to be on the high end of

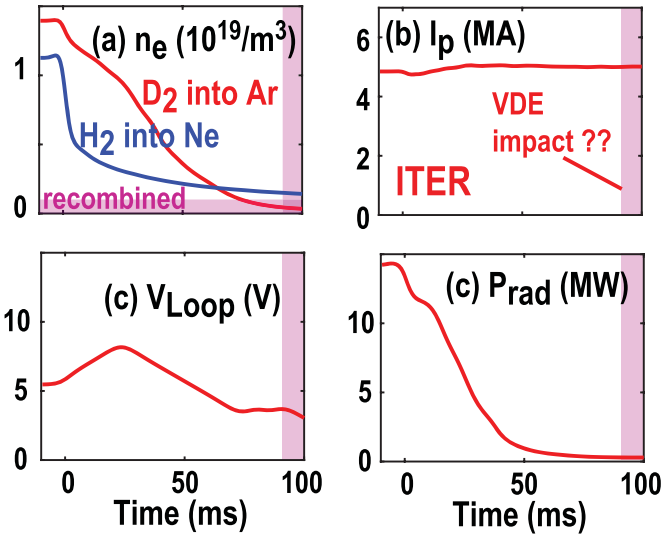

Figure 7. Time traces of RE plateau thermal plasma recombination in ITER showing (*a*) profile-average electron density, (*b*) plasma current, (*c*) loop voltage, and (*d*) radiated power as a function of time. Time is plotted relative to second injection time. Red curves are for 10^4 Torr-L of D_2 into a RE plateau containing 270 Torr-L of Ar, using evolving REs. The blue curve in (*a*) is for 10^4 Torr-L of H_2 into a RE plateau containing 270 Torr-L of Ne, using mono-energetic REs. Plasma current is 5 MA and neutral diffusion scale factor is $D_0 = 5$ in both cases.

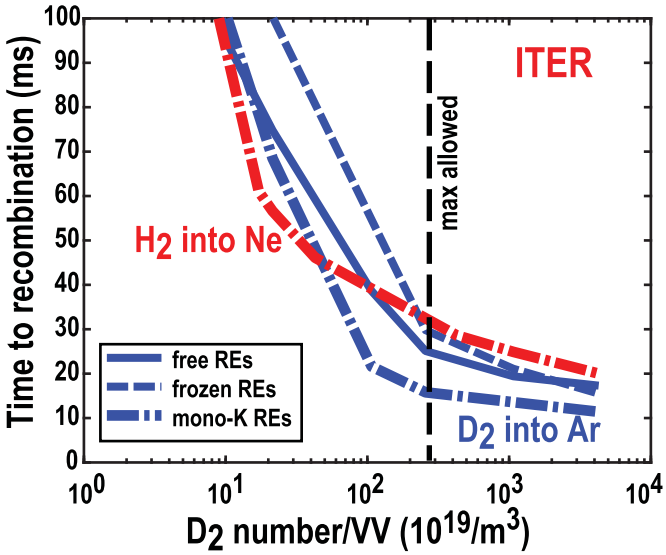

Figure 8. Time to recombination simulated for ITER for 5 MA RE plateaus, starting with 270 Torr-L Ar (or Ne), as a function of injected D_2 (or H_2) number. Blue curves are D_2 fired into an Ar-containing plateau and red curve is H_2 fired into a Ne-containing plateau. All simulations use neutral diffusion scaling $D_0 = 5$.

this range (100 ms) or even longer. For example, if the initial Ne is purged enough to give a factor of 2 decrease in RE plateau effective resistivity, we could expect a VDE impact time of order 100 ms–200 ms (i.e. ∼2× longer). This roughly linear scaling between VDE timescale and effective resistivity is expected to be applicable as long as the timescales are much less than the ITER vessel eddy time (∼500 ms).

Overall, within the uncertainties discussed above, the ITER simulations of figure 7 indicate a time to sufficient recombination of approximately 70 ms in the D_2 into Ar case and a time to sufficient recombination greater than 100 ms in the H_2 into Ne case (for the parameters of figure 7). ITER simulations with different parameters find that the time to achieve sufficient recombination decreases monotonically as more and more D_2 (or H_2) is used during second injection. This is shown in figure 8, which plots simulated time to sufficient recombination for ITER as a function of injected D_2 (or H_2) number. The blue curves are D_2 into Ar cases, while the red curve shows H_2 into Ne cases.

The solid, dashed, and dot-dashed blue curves in figure 8 represent different approximations of the RE energy distribution function. As discussed in section 3, the 1D diffusion model typically uses a 1D (cylindrical) mono-energy/mono-pitch kinetic model and evolves the RE energy and pitch distributions as the D_2 gas diffuses into the RE plasma. Previous work has shown, however, that this kinetic model tends to overestimate the time scale of the RE energy and pitch angle evolution following D_2 injection [26], so it is prudent to ascertain the extent to which uncertainties in the RE energy distribution can affect the simulation results. In figure 8, the solid blue curve uses simulations with the REs evolving according to the kinetic model throughout the simulation. The dashed blue curve corresponds to simulations where the RE energy distribution function is frozen at $t = 0$ and kept fixed after that point. The dot-dashed curve uses the simplest possible energy/pitch distribution, where the REs are just assumed to be mono-energetic (fixed at 1 MeV kinetic energy) and have no pitch angle (the radial shape of the RE density profile from $t < 0$ is still used and the density normalization is obtained by requiring the total current to match the desired value).

5. Equilibrium recombined electron density

The equilibrium recombined cold electron density n_e is seen both experimentally and numerically to be a strong function of the injected D_2 (or H_2) gas quantity. Figure 9 gives examples of equilibrium n_e following D_2 injection for (*a*) DIII-D, (*b*) ITER, (*c*) JET, and (*d*) SPARC. Blue (and green) curves are simulations while black curves/data points are measurements. Here, "equilibrium n_e" is defined as the profile-averaged cold electron density at times $t = 25$, 50, 100, and 20 ms after D_2 (or H_2) gas injection (for DIII-D, JET, ITER, and SPARC respectively). These different times reflect different expected vertical drift timescales in the various devices, i.e. we do not necessarily expect full equilibrium to occur within 20 ms in SPARC, but this is the expected timescale for the RE plateau to drift vertically and hit the wall, so any mixing past this timescale is uninteresting. In JET and DIII-D, the equilibrium n_e reaches a minimum somewhere between 10^{20} and 10^{21} m^{-3} vessel-averaged D_2 number density, and this trend is qualitatively captured by the simulations. The measured rapid n_e rise past this minimum is not well captured in the simulations; the reason for this is not well-understood at present, but could be

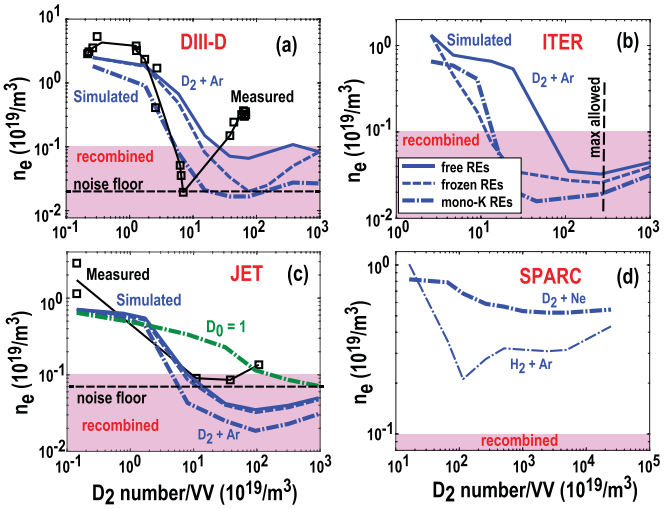

Figure 9. Equilibrium (at $t = 25$ ms for DIII-D, $t = 50$ ms for JET, $t = 100$ ms for ITER, and $t = 20$ ms for SPARC, where t is relative to second injection time) cold thermal electron density as a function of injected D_2 quantity into Ar-containing RE plateaus in (a) DIII-D (with $I_P = 260$ kA and 15 Torr-L Ar), (b) ITER (with $I_P = 5$ MA and 270 Torr-L Ar), (c) JET (with $I_P = 560$ kA and 23 Torr-L Ar), and (d) SPARC (with $I_P = 6$ MA and 33 Torr-L Ar or Ne). All simulations use neutral diffusion scaling $D_0 = 5$, with the exception of the green curve in (c); this uses $D_0 = 1$. Blue curves show simulations: solid lines using evolving REs, dashed lines frozen multi-energy REs, and dot–dash lines frozen mono-energy REs. SPARC simulations show both $D_2 + Ne$ and $H_2 + Ar$ cases; all other cases are only show $D_2 + Ar$.

a result of neutral diffusion/convection changing character at higher densities. For example, the green curve in figure 9(c) shows the simulated equilibrium n_e for mono-energetic REs and using $D_0 = 1$, illustrating a trend toward higher n_e with lower D_0. So if D_0 decreases as more D_2 is injected, this would cause a stronger rise n_e in the simulations. Here, it is not attempted to imply that neutral cooling will go down as neutral number is increased, only that the cooling may not be increasing linearly in this regime. In the example of figure 9(c), it appears that the equilibrium n_e would be better matched in the region $D_2/VV = 10$–100 if D_0 would decrease from 5 to 1. This would imply a roughly $2\times$ increase in neutral cooling over this range, so neutral cooling is still rising as more neutrals are added, but less than linearly.

The solid, dashed, and dot-dashed blue curves in figure 9 represent the same approximations for the RE energy distribution function as discussed for figure 8. Overall, comparison of these different RE energy distribution models in figure 9 suggests that uncertainties in the RE energy distribution can give an error of at most an order of magnitude (typically less) in the equilibrium n_e. These comparisons are important since the model-data comparisons of loop voltage, figures 5(c) and 6(c), indicate that the test particle model systematically underestimates loop voltage (while correctly capturing plasma current). This indicates that power loss from the REs is systematically underestimated by the model, but does not automatically mean that power going into the cold background plasma (which is being studied here) is being systematically underestimated by the same factor. Power put into the REs by the toroidal electric field is dissipated by three terms: stopping power, radial transport, and synchrotron emission and errors could be present in any of these three terms. For the power going into the background plasma, errors in the RE distribution function (at fixed RE current density) typically do not have a dramatic effect on the stopping power loss of relativistic REs, since (a) changes in pitch angle have no effect on stopping power, and (b) changes in kinetic energy only have a small effect on stopping power, as seen in figure 4(c).

6. Effect of plasma current on recombination

As discussed in section 3, the equilibrium recombined n_e is believed to be set dominantly by a balance between molecular recombination and RE impact ionization. Ramping up RE current I_P is expected to increase RE current density, increasing RE impact ionization rate and raising equilibrium n_e. The trend is not strictly linear, since RE current density can be changed by changing RE density, RE energy, or RE pitch angle. The general expected trend is indeed observed experimentally, as shown in figure 10(a), where the equilibrium n_e is plotted from DIII-D as a function of I_P. n_e rises strongly with I_P, rising well above the recombined level at higher I_P values. This basic trend can be seen to be reasonably well captured by the 1D diffusion model, shown by the dot-dashed blue curve in figure 10(a). The fixed mono-energy RE model was used for these simulations.

Figure 10(b) shows equilibrium n_e as a function of injected D_2 (or H_2) number simulated for some different example cases in ITER. Looking at the series of red curves (simulating H_2 injected into Ne-containing RE plateaus), there is a monotonically decreasing trend in equilibrium n_e as I_P is decreased, as expected. Comparing D_2 into Ar with D_2 into Ne with H_2 into Ne, one finds that Ne (vs Ar) increases n_e, while using H_2 (vs D_2) decreases n_e.

7. Effect of initial Ar quantity on recombination

Increasing the amount of injected Ar (or Ne) in the vacuum chamber can be expected to increase stopping power on the REs, resulting in more thermal plasma heating and increasing n_e. However, Ar (or Ne) is largely purged (excluded) from the RE column by secondary massive D_2 (or H_2) injection, so if this purge is perfect, there should actually be no effect. In reality, the purge is not perfect; line-integrated hard x-ray (HXR) measurements suggest a perhaps $10\times$ drop in total Ar density, consistent with modeling [19]. Experimentally, the effect of initial Ar number appears to be small for the ranges of Ar used. Figure 11(a) shows equilibrium n_e measured as a function of Ar number present in JET, indicating no clear effect due to the Ar number; the measured electron density is near the noise floor and the small observed variations are probably within the uncertainty of the measurement. The blue curve in figure 11(a) is from simulations, indicating a small predicted rise in n_e (which is not seen in the scatter of the data, however).

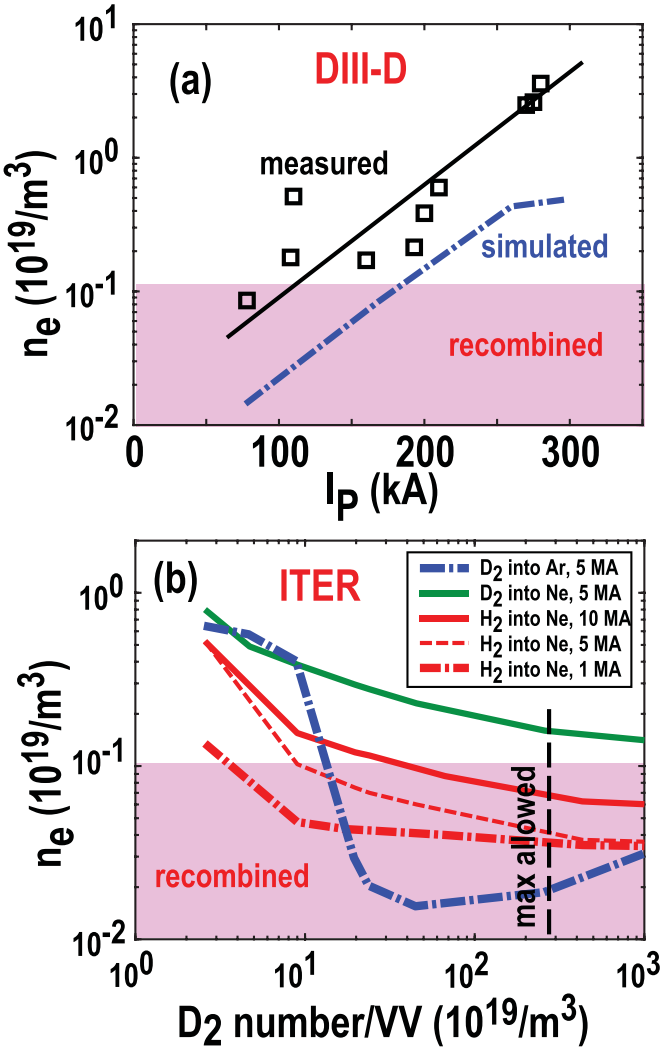

Figure 10. (*a*) Equilibrium (at $t = 25$ ms) electron density n_e as a function of plasma current I_P for DIII-D measured (black curve) and simulated (blue curve) with initial Ar content of 15 Torr-L and 40 Torr-L of injected D_2; and (*b*) equilibrium (at $t = 100$ ms) simulated n_e for ITER as a function of injected D_2 (or H_2) number for D_2 into Ar, D_2 into Ne, and H_2 into Ne with plasma currents $I_P = 1$, 5, and 10 MA. Target Ar (or Ne) quantity is 270 Torr-L. All simulations use frozen, mono-energy REs and diffusion scale $D_0 = 5$.

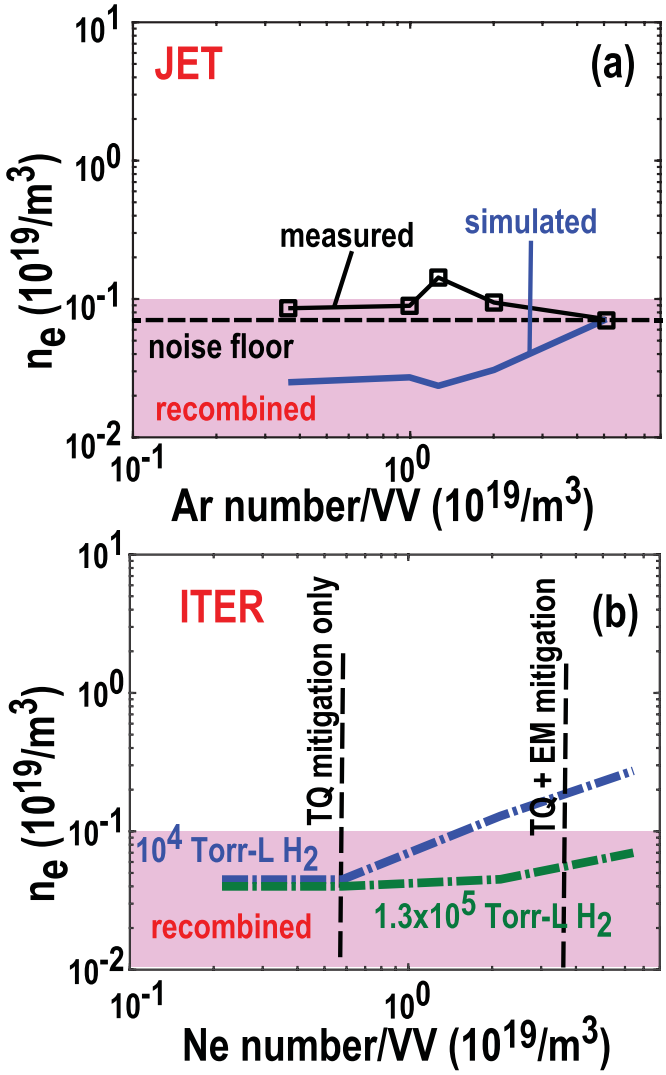

Figure 11. (*a*) Recombined equilibrium (at $t = 50$ ms) electron density n_e as a function of Ar number for JET with 2400 Torr-L D_2 injection and $I_P = 550$ kA. (*b*) Simulated equilibrium (at $t = 100$ ms) electron density n_e as a function of Ne number for ITER with 10^4 Torr-L H_2 injection (blue) or 1.3×10^5 Torr-L H_2 injection (green) and $I_P = 5$ MA. Simulations (blue and green curves) use $D_0 = 5$ and frozen mono-energy REs.

Figure 11(*b*) shows the simulated trend in equilibrium n_e in ITER following H_2 injection, as a function of Ne number, where a slowly rising trend is predicted. The vertical dashed lines in figure 11(*b*) correspond to present expected Ne numbers in ITER expected for TQ heat load mitigation only or for TQ heat load + electro-magnetic load mitigation [27]; presumably, plasma current at the time of the disruption will determine which of these two cases is used. For the larger Ne quantity, the equilibrium n_e is predicted to rise enough to come out of the 'recombined' region. The injected H_2 quantity in the simulations of figure 11(*b*) are at the ITER 'optimum' of 10^4 Torr-L H_2 (blue curve) and for the 'max allowed' around 1.3×10^5 Torr-L H_2 (green curve). Injecting the maximum allowed quantity of H_2 is predicted to bring n_e into the recombined region (even for the largest expected Ne quantity) at 5 MA RE current.

We note here that final loss instability characteristics can be different depending on the amount of neon or argon in the vacuum vessel. We only focus here on equilibrium electron density, but JET data shows that recombined discharges with different argon numbers in the vessel can behave quite differently during the final loss instability [28]. The lack of dependence in n_e vs Ar (or Ne) number of figure 11 should therefore not be interpreted as meaning there is no difference in resulting final wall damage as Ar (or Ne) number are varied.

8. Discussion

The present work is a small step in the ongoing research toward determining which approach will be more likely to prevent serious RE wall strike wall damage in ITER—massive high-Z injection into the RE plateau or massive low-Z injection into the RE plateau. Massive high-Z injection has intuitive appeal in that it attempts an immediate rapid increased dissipation of RE current, while massive low-Z injection uses a less intuitive approach: increasing RE current, while anticipating larger final loss MHD, with greater resulting spreading of RE impacts on the wall and lower conversion of magnetic energy to kinetic energy. In evaluating the potential effectiveness of the low-Z approach, a necessary first step is being able to predict if sufficient RE background plasma recombination will occur, since this appears to be an important element in enabling large global MHD during the RE plateau wall strike. The present work suggests that use of Ne for TQ and CQ mitigation will make achieving sufficient recombination more difficult (when compared to Ar). As the Ne quantity is turned up, achieving recombination becomes harder and harder (although slowly), as shown in figure 11(*b*). As expected, larger RE plateau plasma current densities make achieving RE plateau plasma recombination more and more difficult, as shown in figure 10(*a*). At $I_P = 10$ MA, achieving recombination in ITER is expected to be barely possible, within injection quantity limits, as shown in figure 10(*b*). In SPARC, with its very high current densities, achieving sufficient recombination may be impossible, especially if Ne and D_2 are used. With Ar and H_2, it appears that there may be some possibility of achieving recombination, figure 9(*d*), especially if a lower-current RE plateau occurs (in figure 9(*d*), a near-worst-case scenario of 6 MA RE current is simulated). As shown in figure 8, timescales for achieving sufficient recombination in ITER typically appear to be fast enough to beat the vertical instability timescale, assuming that sufficient H_2 (or D_2) is injected.

The 1D model used here suggests that achieving RE plateau recombination will be harder in the presence of background Ne instead of Ar, figure 10(*b*). The source of this difference is Ne vs Ar plasma chemistry, where 'chemistry' here refers to neon interactions with thermal plasma, including ionization, recombination, charge-exchange, etc. In particular, recombination of neon ions via molecules is predicted to be slower than for Ar, due to the much slower rate of neon deuteride formation by impact with D_2 molecules. As discussed above, particle balance after D_2 injection is set dominantly by RE-impact ionization balanced by molecular recombination, so slowing down molecular recombination will make achieving RE plateau recombination more difficult. Other differences between Ne and Ar include stopping power and diffusion. Neon has a lower stopping power on REs, resulting in lower background plasma heating and a lower ionization rate; these differences will tend to make recombination easier. Neon neutrals will also tend to diffuse faster than Ar neutrals; this will also tend to make recombination easier, since neon can form a hollow neutral profile more quickly than Ar. These trends are illustrated in figure 12, where equilibrium n_e is predicted for ITER

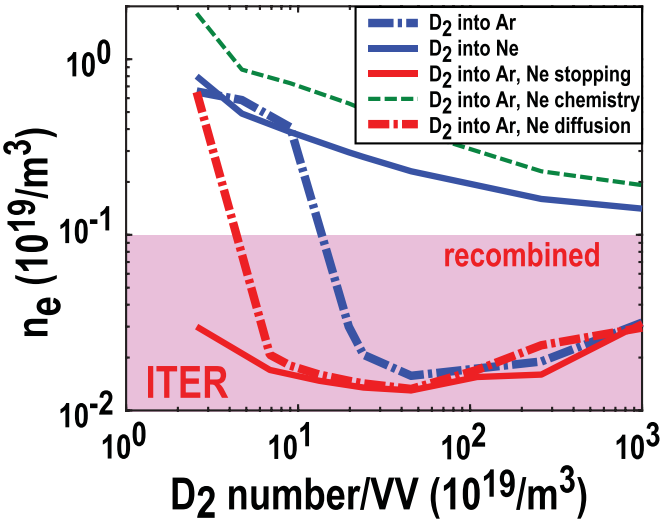

Figure 12. Equilibrium (at $t = 100$ ms) simulated n_e for ITER as a function of injected D_2 number for D_2 into Ar (or Ne) with $I_P = 5$ MA. Target Ar (or Ne) quantity is 270 Torr-L. All simulations use frozen, mono-energy REs and diffusion scale $D_0 = 5$. Red and green curves are simulations using Ar but with Ne stopping power, Ne chemistry, or Ne diffusion turned on.

as a function of D_2 number. The solid blue curve gives the prediction for D_2 into Ne, while the dot–dash blue curve gives the prediction for D_2 into Ar; these curves were already shown in figure 10(*b*). The green dashed curve shows D_2 into Ar but with Ne chemistry, showing higher n_e than even for D_2 into Ne. The red solid curve shows D_2 into Ar but with Ne stopping power, showing a decrease in n_e. Similarly, D_2 into Ar but using Ne diffusion (red dot–dash curve) shows a decreasing trend in n_e. Overall, the prediction for Ne is that its stopping power and diffusion will tend to help recombination, but this is more than offset by the Ne chemistry, which will tend to make recombination harder. Other high-Z first injection background species (other than Ne or Ar) are not considered here, since Ne and Ar were the only species under consideration for first injection in ITER. Also, experimentally, low-Z second injection experiments have presently only been performed into RE plateaus with Ne or Ar present from first injection, although high-Z second injection of other species such as Kr or Xe has been attempted in previous experiments in JET [7].

Going forward, many areas of improvement are possible in this topic. The present diffusion model is 1D only; however, toroidally resolved measurements have shown that the RE plateau neutral and ion transport is fully 3D, due to the very low temperatures, high collisionality, and long toroidal distances [11]. In contrast, the present work just assumes a 0D (constant in time and space) ion diffusion coefficient and a 1D (radially varying) neural diffusion coefficient which is scaled by a 0D (constant in space and time) scaling parameter $D_0 = 5$. The accuracy of these approximations for ITER or SPARC have not been investigated. The main purpose of this work is to estimate equilibrium line-integrated electron density after low-Z second injection; this is captured within a factor of 2 by this model in DIII-D and JET, as seen in figures 9(*a*), (*c*), 10(*a*),

and 11(*a*). It can be hoped that a similar predictive accuracy applies to ITER and SPARC, but this remains to be determined [11] is figures 9(*a*), (*c*), 10(*a*), and 11(*a*). Similarly, recombination timescales are predicted (with scaled D_0) within a factor of 2, as shown in figures 5(*a*) and 6(*a*), but the accuracy of this model for ITER and SPARC is still undetermined. As shown in figure 9, the error bars associated with the RE kinetic model used here are quite large, about an order of magnitude. Improved RE modeling is therefore needed to more accurately capture the ionization and heating from REs acting on the cold background plasma. In figures 5 and 6, the present model only captures the experimental loop voltages in DIII-D and JET very coarsely (within a factor of 5), indicating a significant level of disagreement between the modeled and experimental RE and impurity distribution. Another area of significant disagreement is the radiated power in JET: in DIII-D the RE plateau radiated power is observed to drop following low-Z injection, while in JET it appears to rise, as shown in figure 6(*d*). This trend is not captured by the present modeling, and needs to be understood to improve confidence in these simulations. Presently, it is not clear if this disagreement comes from 3D effects, incorrect radiation rate coefficients, or something else. In the JET bolometer data, clear indications of spatial structure can be seen in the view chords, in both vertical and horizontal bolometer fans, with a peak in radiated power near the magnetic axis. This suggests that it is unlikely that inversion errors (e.g. incorrectly weighting divertor channels) can account for the discrepancy, especially since inverted total radiated power is not typically strongly sensitive to inversion model details and similar radiated power levels are obtained from two different bolometer fans. Also, the clear indications of spatial structure suggest that neutral heating of the bolometer foils (which should affect all channels) is not causing an erroneously large radiated power signal. In the present 1D model, the radiation rates for RE impact on D_2 molecules are estimated by merging low-temperature (up to 100 eV) collisional-radiative thermal plasma simulations [29] to mono-energetic relativistic (MeV) stopping power data [30], with thermal and RE components considered separable. This method does not self-consistently model simultaneous RE and thermal excitation and may not be completely accurate. Radiation trapping from D_2 molecules is not included in the model, but preliminary estimates suggest that this is not a large effect, causing at most a factor of 2 reduction in D_2 radiated power for ITER (less for smaller machines).

9. Summary

In summary, efforts were made to match trends seen in RE plateau thermal plasma partial recombination following massive D_2 injection in DIII-D and JET tokamaks and extrapolate to ITER and SPARC using a 1D diffusion model. Basic trends seen in the experiments are reproduced in the 1D model, including: (a) a drop in equilibrium electron density n_e with increasing D_2 injection quantity, (b) a rise in n_e with increasing plasma current I_P, and (c) only a weak dependence of n_e on the initial Ar quantity. Extrapolation to ITER suggests that (within the approximations of this model) sufficient RE plateau recombination by massive H_2 injection should be possible on the vertical drift timescale if the plasma current is not too high. Extrapolation to SPARC suggests that sufficient RE plateau recombination will be more challenging there, especially if D_2 into Ne is used, but may be achievable if H_2 into Ar is used.

Appendix . Addition of H^-, Ne and H_2 to RE plateau 1D neutral diffusion model

The 1D neutral diffusion model used here was mostly described previously, in appendix of [10], as well as appendix of [19]. For brevity, we only describe changes made to the previous model. The main changes made involve adding H^- ions (to improve the accuracy of the molecular recombination rate), and neon and hydrogen, to allow modeling of neon-containing plasmas (instead of Ar) and modeling of H_2 injection (instead of D_2).

(a) Addition of $\mathbf{H}^-$ ions
Three processes involving the H^- ion are added: formation by electron impact, destruction by electron impact, and recombination; other processes involving H^- are believed to be less important and are neglected. Rate coefficients are taken from [29]. For reaction (A1), the strong D_2 vibrational temperature dependence is not modeled explicitly; instead, this is encapsulated in a T_e dependence, as done in [29],

$$e + D_2 \rightarrow D + D^- \tag{A1}$$

$$e + D^- \rightarrow 2e + D \tag{A2}$$

$$D^- + D^+ \rightarrow 2D. \tag{A3}$$

(b) Substituting neon for argon
To run a neon-containing target plasma instead of argon, the effect on the RE distribution function due to reduced scattering is included. Smaller effective ionization potentials from [31] are used for these reduced stopping powers of different charge states and nuclear log lambdas (Coulomb collisions parameters) are adjusted for neon for the purposes of pitch angle scattering.

The following reactions are neglected, because their rate coefficients are believed to be small, $S < 10^{-14}\mathrm{cm}^3\mathrm{s}^{-1}$ [32]:

$$Ne^+ + D_2 \rightarrow NeD^+ + D \tag{A4}$$

$$D_2^+ + Ne \rightarrow D_2 + Ne^+ \tag{A5}$$

$$D + Ne^+ \rightarrow D^+ + Ne \tag{A6}$$

$$D_2 + Ne^+ \rightarrow D_2^+ + Ne. \tag{A7}$$

Recombination rates of Ne ions are made using standard rates for three-body and radiative recombination [33] and then adding in dielectronic recombination rates [34].

The dominant neon deuteride ion formation channels are included:

$$D_3^+ + Ne \rightarrow NeD^+ + D_2 \tag{A8}$$

$$D_2^+ + Ne \rightarrow NeD^+ + D. \tag{A9}$$

The rate coefficient for (A8) is approximated from the from the rate for NeD^+ formation from $D_2^+ + Ne$, by the scaling with ratio of $D_3^+ + Ar$ over $D_2^+ + Ar$ rates for ArD^+ formation [32]. The rate coefficient for (A9) is estimated from [32].

Thermal plasma ionization rates, e.g. $Ne + e \rightarrow Ne^+ + 2e$ is estimated from optically thick CRETIN calculations [35]. As for Ar, higher charge state ionization is typically dominated by RE impact (not thermal electron impact). RE ionization is estimated from the relativistic ionization rate of neutral atoms from [30], reduced for higher charge states using effective ionization potential values [31] and including the enhancement factor for Auger excitation [36].

The following reactions starting with the neon deuteride ion are included:

$$NeD^+ + D_2 \rightarrow D_3^+ + Ne \tag{A10}$$

$$NeD^+ + e \rightarrow Ne + D \tag{A11}$$

$$NeD^+ + e \rightarrow Ne^+ + D + e. \tag{A12}$$

The rate coefficient for (A10) is taken from [32]. The rate coefficients for (A11) and (A12) are estimated from the data of [37]; (A11) is taken from the first data peak, while (A12) is taken from the second peak in the data.

The following charge-exchange reactions involving higher charge states of neon are included:

$$D_2^+ + Ne^{2+} \rightarrow 2D^+ + Ne^+ \tag{A13}$$

$$Ne^{2+} + D_2 \rightarrow Ne^+ + D_2^+ \tag{A14}$$

$$Ne^{3+} + D \rightarrow Ne^{2+} + D^+ \tag{A15}$$

$$Ne^{3+} + D_2 \rightarrow Ne^{2+} + D_2^+ \tag{A16}$$

$$Ne^{4+} + D \rightarrow Ne^{3+} + D^+ \tag{A17}$$

$$Ne^{4+} + D_2 \rightarrow Ne^{3+} + D_2^+. \tag{A18}$$

For reaction (A13), an simple average of analogous reactions involving He^{2+} and Ar^{2+} is used [38]. For reactions (A14)–(A18), the rate coefficients are estimated from the higher-energy measurements of [39] by extrapolating to lower energy.

(c) Substituting H_2 for D_2

To simulate injection of H_2 instead of D_2, it is assumed that cross sections are the same for inelastic collisions (such as charge exchange), but the rate coefficients are updated using the faster thermal velocity of H_2. Electron-impact collision rates are assumed unchanged, since the electron velocity is fast compared with both H_2 and D_2. For elastic collisions, cross sections are updated using the correct neutral polarizability (H or H_2 instead of D or D_2) for ion-neutral elastic scattering and using the correct effective radius for momentum scattering for neutral-neutral collisions [40–42]. Mixed-species (simultaneous treatment of both H and D) diffusion is not done, since the injected species typically dominates in number over the initial atom quantity, so only single hydrogenic species simulations are done (i.e. if H_2 second injection is simulated, it is assumed that the initial hydrogenic content of the plasma is also H rather than D).

Acknowledgments

This material is based upon work supported by the U.S. Department of Energy, Office of Science, Office of Fusion Energy Sciences, using the DIII-D National Fusion Facility, a DOE Office of Science user facility, under Award(s) DE-FG02-07ER54917, DE-FC02-04ER54698, DE-AC05-00OR22725, DE-AC52-07NA27344, DE-FG02-04ER54744, DE-SC0020296, DE-SC0020299, DE-SC0022270, and DE-AC05-06OR23100. R Sweeney was supported in part by Commonwealth Fusion Systems. Technical support of the DIII-D and JET experimental teams is gratefully acknowledged. Diagnostic support of M Van Zeeland is acknowledged. Permission to use CRETIN from H A Scott is gratefully acknowledged. **Disclaimer:** This report was prepared as an account of work sponsored by an agency of the United States Government. Neither the United States Government nor any agency thereof, nor any of their employees, makes any warranty, express or implied, or assumes any legal liability or responsibility for the accuracy, completeness, or usefulness of any information, apparatus, product, or process disclosed, or represents that its use would not infringe privately owned rights. Reference herein to any specific commercial product, process, or service by trade name, trademark, manufacturer, or otherwise does not necessarily constitute or imply its endorsement, recommendation, or favoring by the United States Government or any agency thereof. The views and opinions of authors expressed herein do not necessarily state or reflect those of the United States Government or any agency thereof. **Disclaimer 2:** This work has been carried out within the framework of the EUROfusion Consortium, funded by the European Union via the Euratom Research and Training Programme (Grant Agreement No. 101052200—EUROfusion). Views and opinions expressed are however those of the author(s) only and do not necessarily reflect those of the European Union or the European Commission. Neither the European Union nor the European Commission can be held responsible for them.

ORCID iDs

E.M. Hollmann https://orcid.org/0000-0002-6267-6568
N.W. Eidietis https://orcid.org/0000-0003-0167-5053
J.L. Herfindal https://orcid.org/0000-0003-2846-597X
A. Lvovskiy https://orcid.org/0000-0002-3649-1169
C. Paz-Soldan https://orcid.org/0000-0001-5069-4934
C. Reux https://orcid.org/0000-0002-5327-4326
R. Sweeney https://orcid.org/0000-0003-3408-1497

References

[1] Nygren R., Lutz T., Walsh D., Martin G., Chatelier M., Loarer T. and Guilhem D. 1997 *J. Nucl. Mater.* **241** 522–7
[2] Hender T.C. *et al* 2007 *Nucl. Fusion* **47** S128
[3] Matthews G.F., Bazylev B. and Baron-Wiechec A. 2016 *Phys. Scr.* **2016** 014070
[4] Hollmann E.M. *et al* 2013 *Nucl. Fusion* **53** 083004
[5] Hollmann E.M. *et al* 2015 *Phys. Plasmas* **22** 021802
[6] Shiraki D., Commaux N., Baylor L.R., Cooper C.M., Eidietis N.W., Hollmann E.M., Paz-Soldan C., Combs S.K. and Meitner S.J. 2018 *Nucl. Fusion* **58** 056006
[7] Reux C. *et al* JET contributors 2015 *Nucl. Fusion* **55** 129501
[8] Lehnen M. *et al* EFDA JET Contributors 2015 *J. Nucl. Mater.* **463** 39
[9] Breizman B.N., Aleynikov P., Hollmann E.M. and Lehnen M. 2019 *Nucl. Fusion* **59** 083001
[10] Hollmann E.M. *et al* 2019 *Nucl. Fusion* **59** 106014
[11] Hollmann E.M. *et al* 2022 *Phys. Plasmas* **29** 022503
[12] Martin-Solis J.R., Loarte A., Hollmann E.M., Esposito B. and Riccardo V. FTU and DIII-D Teams and JET EFDA Contributors 2014 *Nucl. Fusion* **54** 083027
[13] Hollmann E.M., Commaux N., Eidietis N., Lasnier C.J., Rudakov D.L., Shiraki D., Cooper C., Martin-Solis J.R., Parks P.B. and Paz-Soldan C. 2017 *Phys. Plasmas* **24** 062505
[14] Paz-Soldan C., Eidietis N.W., Liu Y.Q., Shiraki D., Boozer A.H., Hollmann E.M., Kim C.C. and Lvovskiy A. 2019 *Plasma Phys. Control. Fusion* **61** 054001
[15] Reux C. *et al* 2021 *Phys. Rev. Lett.* **126** 175001
[16] Paz-Soldan C. *et al* 2021 *Nucl. Fusion* **61** 116058
[17] Jachmich S. *et al* 2021 *Nucl. Fusion* 02601**62**
[18] Creely A., Greenwald M. and Ballinger S. 2020 *J. Plasma Phys.* **86** 5
[19] Hollmann E.M. *et al* 2020 *Phys. Plasmas* **27** 042515
[20] Carlstrom T.N., Ahlgren D.R. and Crosbie J. 1988 *Rev. Sci. Instrum.* **61** 2865
[21] Boboc A., Bieg B., Felton R., Dalley S. and Kravtsov Y. 2015 *Rev. Sci. Instrum.* **86** 091301
[22] Martin-Solis J.R., Alvarez J.D., Sanchez R. and Esposito B. 1998 *Phys. Plasmas* **5** 2370
[23] Chapman S. and Cowling T.G. 1970 *The Mathematical Theory of Non-Uniform Gases* 3rd edn (Cambridge, MA: Cambridge Mathematical Library)
[24] Frolov B.K., Pigarov A.Y., Krasheninnikov S.I., Petzoldt R.W. and Goodin D.T. 2005 *J. Nucl. Mater.* **337** 206
[25] Kiramov D.I. and Breizman B.N. 2017 *Phys. Plasmas* **24** 100702
[26] Popovic Z., Hollmann E.M., Del-castillo-negrete D., Bykov I., Herfindal J.L., Shiraki D., Eidietis N.W., Paz-Soldan C. and Lvovskiy A. 2021 *Phys. Plasmas* **28** 082510
[27] Lehhen M. 2021 *The ITER Disruption Mitigation System—Design Progress and Design Validation* (Princeton, NJ: Princeton Workshop on Theory and Simulations of Disruptions)
[28] Reux C. *et al* 2022 *Plasma Phys. Control. Fusion* **64** 034002
[29] Janev R.K., Reiter D. and Samm U. 2003 Collision processes in low-temperature hydrogen plasmas *FZJ Report JUEL-415* (available at: https://juser.fz-juelich.de/record/38224/files/Juel_4105_Reiter.pdf)
[30] Rieke F.F. and Prepejchal W. 1972 *Phys. Rev.* A **6** 1507
[31] Sauer S.P.A., Oddershede J. and Sabin J.R. 2015 *Adv. Quantum Chem.* **71** 29
[32] Anicich V.G. 1993 *J. Phys. Chem. Ref. Data* **22** 1469
[33] Huba J.D. 2002 *NRL Plasma Formulary* (Washington, DC: Plasma Physics Division, Naval Research Laboratory)
[34] Jacobs V.L., Davis J., Rogerson J.E. and Blaha M. 1979 *Astrophys. J.* **230** 627
[35] Scott H.A. 2001 *J. Quant. Spectrosc. Radiat. Transfer* **71** 689
[36] Salop A. 1974 *Phys. Rev.* A **9** 2496
[37] Mitchell J.B.A., Novotny O., Angelova G., LeGarrec J.L., Rebrion-Rowe C., Svendsen A., Andersen L.H., Florescu-Mitchell A.I. and Orel A.E. 2005 *J. Phys. B* **38** 693
[38] Brauning H., Reiser I., Diehl A., Theiss A., Sidky E., Cocke C.L. and Salzborn E. 2001 *J. Phys.* B **34** L321
[39] Can C., Gray T.J., Varghese S.L., Hall J.M. and Tunnell L.N. 1985 *Phys. Rev.* A **31** 72
[40] Ambdur I., Kells M.C. and Davenport D.E. 1950 *J. Chem. Phys.* **18** 1676
[41] Phelps A.V. 1992 *J. Phys. Chem. Ref. Data* **21** 883
[42] Osterbrock D.E. 1961 *Astrophys. J.* **134** 270